



1 **Distance of flight of cosmic-ray muons to study dynamics of the**

2 **upper muosphere**

3

4 Hiroyuki K.M. Tanaka^{1,2*}

5

6 1. University of Tokyo, Tokyo, Japan.

7 2. International Virtual Muography Institute (VMI), Global, Tokyo, Japan.

8

9 Correspondence to: Hiroyuki K.M. Tanaka

10

11 **Abstract**

12 The Earth can be divided by main layers, including the atmosphere, geosphere (solid
13 Earth), and biosphere, depending on its predominant component. In this work, the layer
14 of the Earth which constantly contains a high concentration of muons ($\sim 8 \times 10^{12}$ muons)
15 and its upper border are respectively defined as the muosphere and muopause. The
16 altitude of the muosphere spans from the lower stratosphere to the upper crust of the Earth.
17 In order to study its dynamics, the muopause height was spatiotemporally studied with a
18 new kind of technique called the distance of flight (DoF) which utilizes variations in the
19 muon's decay length. In this work, (A) numerical modeling was performed, and it was
20 clarified that seasonal variations in the cosmic muon flux are predominantly ruled by
21 muopause dynamics, (B) the muon data were compared with the balloon-based
22 measurement results, and it was confirmed that muopause dynamics is closely related
23 with lower-stratospheric height variations. Since the muopause is the region spanning
24 between the upper troposphere and the lower stratosphere, the potential of the current
25 DoF approach needs to be further investigated by cross-comparing related case studies
26 and other atmospheric climate datasets.

27

28 **Introduction**

29 The Earth can be divided into its main layers including the atmosphere, geosphere (solid
30 Earth), biosphere, depending on its predominant component: gas in the atmosphere, solid
31 rock/metal in the geosphere, biological activities in the biosphere. Muons are secondary
32 particles generated in the Earth's atmosphere as a result of hadronic interactions between
33 the incident primary cosmic rays (primaries) and atmospheric nuclei such as nitrogen and
34 oxygen. These primaries usually do not interact with matter within the top region of the



35 Earth's atmosphere due to the low number density of atmospheric nuclei. However, as
36 primaries' injection depth increases, the density of the atmosphere increases, and these
37 primaries start to interact with nuclei, producing mesons such as charged pions and kaons
38 which eventually decay into muons. Once these mesons decay into muons, there will
39 generally be no further interaction to generate new particles since muons do not strongly
40 interact with matter. Therefore, muons are extensively produced within particular altitude
41 regions of the atmosphere. The muons' production rate increases as a function of the
42 atmospheric depth such that: <0.01%, ~0.2%, ~2%, ~30%, and ~80% (of the entire
43 muons we observe at sea level) up to an atmospheric depth of 5 hPa, 10 hPa, 50 hPa, 100
44 hPa, and 200 hPa, respectively, and almost all muons are generated up to an atmospheric
45 depth of 300 hPa (Particle Data Group, 2022; Boezio *et al.*, 1999; Boezio *et al.*, 2000).
46 On the other hand, due to its strong penetration power, the muons also exist in the
47 geosphere with a rock/water depth up to ~5/~10 km. Consequently, muons are
48 predominant in the region defined on the altitude coordinate as ranging from 30 km and
49 -10 km which also partly overlaps with regions of the humanosphere. This region (from
50 +30 km to -10 km from sea level) is here defined as the muosphere. Accordingly, the
51 muopause is defined as the upper boundary of the muosphere (as with the tropopause
52 defining the upper boundary of the troposphere) which is located at 30 km asl. The key
53 characteristics of the muons within the muosphere are: (A) an abundance of $\sim 8 \times 10^{12}$
54 muons ($(1.6 \times 10^2 \text{ m}^2\text{s}^{-1})$ [averaged muon flux] $\times (5 \times 10^{14} \text{ m}^2)$ [Earth's surface area] \times
55 $(3.5 \times 10^4 \text{ m})$ [thickness of the muosphere] / $(3 \times 10^8 \text{ ms}^{-1})$ [speed of muons]) with a
56 concentration of $\sim 5 \times 10^3$ muons km^{-3} are constantly present in the muosphere, (B) $\sim 8 \times$
57 10^{16} muons are generated in the muosphere every second and (C) $\sim 5 \times 10^{16}$ muons arrive
58 at sea level every second. The exception to this would be neutrino-induced muons which
59 exist throughout the geosphere (Particle Data Group, 2022), but the concentration of these
60 neutrino-induced particles within the geosphere is too small ($< 10^{-9}$ muons km^{-3}) to
61 categorize them as being part of the muosphere.

62

63 The thickness of the muosphere spatiotemporally fluctuates due to processes near the
64 surface of the Earth: mainly crustal deformation and land temperature variations. Crustal
65 deformation alters the density of the shallow crust and local topography. When this occurs,
66 the underground depth threshold for muons to reach will be altered; hence the position of
67 the bottom part of the muosphere is regionally altered, but the time scale of this change
68 is very long (over millennia). On the other hand, the near-surface temperature variations
69 will alter the isobaric surface height near the muopause in much shorter time scales.

70



71 Since muopause height variations are closely related with the upper-tropospheric and
72 lower-stratospheric isobaric surface height variations. Studying muopause dynamics has
73 the potential to contribute to research in this field. For example, it was reported that the
74 2020 and 2021 ozone holes were both associated with large decreases in polar lower
75 stratospheric heights (Yook *et al.*, 2022). SSWs are characterized by large geopotential
76 height rises at the pole (Kretschmer *et al.*, 2018). The 2022 Hunga Tonga–Hunga Ha’apai
77 volcano eruption, Tonga resulted in a substantial injection of water vapor into the upper
78 atmosphere (Millán *et al.*, 2022; Vömel *et al.*, 2022). Such changes in the atmospheric
79 composition should have had a noticeable impact on the muopause.

80

81 The established muographic imagery techniques have been applied to natural phenomena
82 such as volcanoes (Tanaka *et al.*, 2014), cultural heritage (Morishima *et al.*, 2017), tropic
83 cyclones (Tanaka *et al.*, 2022a), meteotsunami (Tanaka *et al.*, 2022b), and contraband
84 detection (Gnanvo *et al.* 2011). These techniques take advantage of known properties of
85 muon transmission and scattering through matter. In this work, the DoF technique is
86 added, and it will be shown that the muopause height variations can be measured with
87 this technique based on the quantitative analysis of the time-sequential muon data. Since
88 muons are leptons with a decay constant of 2.2 microseconds, the distance traveled has
89 an influence on the muon’s survival rate. Consequently, the sea-level muon flux will
90 decrease/increase as the muopause uplifts/lowers. This is the basic principle of the DoF
91 approach. In this work, the aim was to show balloon-based lower stratospheric height
92 variations are well reproduced by applying the DoF approach to the time-sequential muon
93 observation data.

94

95 There are a number of reports exploring barometric and temperature effects in the muon
96 flux (Tanaka *et al.*, 2022a; Tilav *et al.* 2010; COSINE-100 Collaboration, 2020;
97 Myssowsky and Tuwim *et al.* 1926; Blackett, 1938; The IceCube Collaboration, 2019;
98 Adamson *et al.*, 2010) including a recent detailed review (Dmitrieva *et al.* 2011).
99 However, many of these works focus on either tropospheric barometric effect or
100 stratospheric temperature effect. In this work, DoF approach was modeled and applied to
101 the 1,044-day time sequential muon data to compare with the Japan Meteorological
102 Agency’s balloon data.

103

104 As a result, the following three major characteristics were identified: (A) seasonal
105 variations in the muon flux due to the isobaric surface height effect are much larger than
106 seasonal variations due to the barometric effect, therefore, (B) the isobaric surface height



107 derived by the DoF technique is consistent with the balloon-based upper-atmosphere
108 isobaric surface height measurement results. In this paper, a detailed description of the
109 process to arrive these results is provided. A brief discussion of its current limitation and
110 potential improvements are also described.

111

112 **2. Principle of the DOF technique**

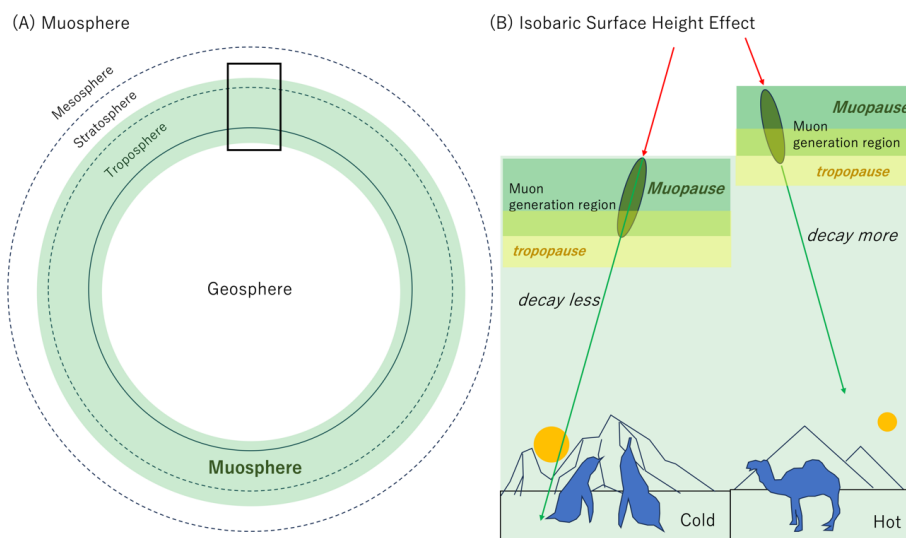
113 The atmospheric cascades of secondary pions and kaons are developed as a result of the
114 competition between the hadronic process and the decay process in the atmosphere.
115 Therefore, muons are not generated at a specific altitude, but instead they are generated
116 within a certain altitude range (Boezio *et al.*, 1999; Boezio *et al.*, 2000).

117

118 Figure 1 shows the layer span of the muosphere on the Earth and the principle of the DoF
119 technique. As shown in Figure 1A, the muosphere covers the region from the lower
120 stratosphere, troposphere, and shallow region of the geosphere (shallow crust and ocean).
121 Topography of the muopause is determined by the isobaric surface height distribution of
122 the upper atmosphere, and is generally related to the height of tropopause. However, the
123 tropopause region does not usually overlap with the muopause region. The isobaric
124 surface height is high when the surface temperature is high and low in when the surface
125 temperature is low since the larger vertical temperature gradient causes deeper convection
126 in the troposphere, pushing the isobaric surface, upwards; hence seasonally varied. More
127 detail descriptions can be found later in the “Balloon-based studies near the muopause”
128 section. As shown in Figure 1B, variations in the height of the muopause will affect the
129 muon generation point; hence the muon’s DoF. The number of muons decreases when the
130 muopause is uplifted. If the isobaric surface height effect is comparable to or stronger
131 than the barometric effect on the muon flux, the spatiotemporal variations in the
132 muopause can be measured by using the local barometric data. Detailed descriptions
133 about two essential aspects of the DoF technique, (1) modelling of the seasonal
134 barometric effect on the muon flux and (2) modelling of the seasonal isobaric surface
135 height effect on the muon flux, are given in the following subsections.

136

137



138
139
140
141
142
143
144
145
146
147
148

Figure 1. Definition of muosphere and the principle of the DOF technique. The span of the muosphere is shown along with other layers of the Earth (A). The black box indicates the muosphere for the region shown in (B). Red arrows and green arrows respectively indicate the primary cosmic rays and muons. Additionally, (B) shows an example of the contrast between the average height of the muopause above colder surface temperature and the height of the muopause above warmer surface temperature. Dark green ovals indicate the muon production regions. As is indicated with yellow-filled boxes, the tropopause and the muopause do not exactly overlap with each other.

149 3. DoF Modeling

150 3.1 Modeling of the seasonal barometric effect on muon flux

151 The cosmic muon flux is also influenced by ground-level barometric variations because
152 the amount of muon energy loss depends on the total areal density along their trajectories.
153 In this work, we took advantage of muon flux variations associated with the presence of
154 a cyclone to derive variations in the muon counts in the detector as a function of the
155 ground-level pressure in Kagoshima city. The advantage of using the cyclone data is that
156 since the cyclone moves quickly (typically within 24 hours) and will dramatically alter
157 the ground-level atmospheric pressure (sometimes by more than 40 hPa), barometric
158 muon flux variations can be evaluated without being influenced from the longer-time-
159 scale isobaric surface height effect. Figure 2A compares the temporal variations in the
160 muon flux and the temporal variations in the ground-level atmospheric pressure induced

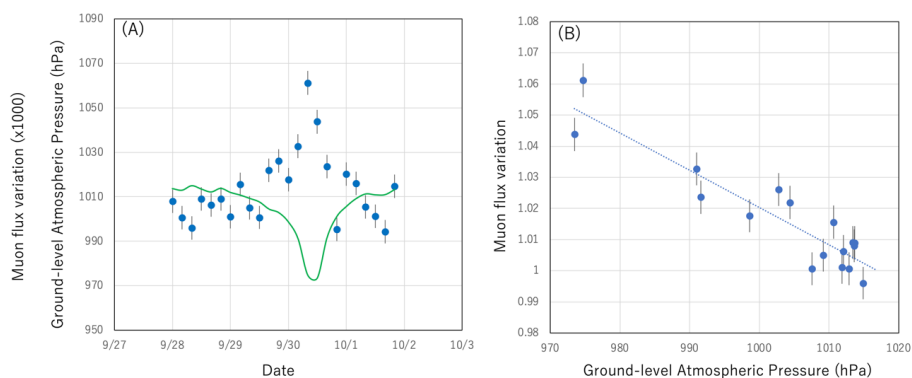


161 by the 2018 Typhoon No 24. Figure 2B shows the relationship between the muon flux
162 and the atmospheric pressure (both measured in Kagoshima city). The metrological data
163 in Figure 2 were taken from Reference (Japan Metrological Agency, 2023). The data
164 points were fitted by a linear function and the result is shown in the following equation:

$$165 \Delta N = 0.0012 \Delta P [\text{hPa}] + 2.2159. \quad (1)$$

166
167
168 This result indicates that the muon flux varies by 1.2% if the ground-level atmospheric
169 pressure changes by 10 hPa. Since the detector used for measuring this cyclone effect on
170 the muon flux is identical to that used for the DoF measurements, the external factors
171 including the zenith angular dependence of the muon flux, geometrical acceptance of the
172 detector, etc. are canceled out. The fractions of the number of the data points are
173 respectively 60%, 82%, and 100% for deviations of $\leq 1\sigma$, $\leq 1.5\sigma$, and $\leq 2\sigma$ from the
174 estimated line. The SD of the data points from the estimated line (0.0065) which is close
175 to the statistical error associated with the data points (0.0052-0.0054). The difference
176 between them (0.0037) can be the fitting uncertainty which adds an uncertainty of ~ 18 m
177 in estimation of the muopause height (See below). Eq. (1) was used for the barometric
178 correction to the muon flux in the current work.

179



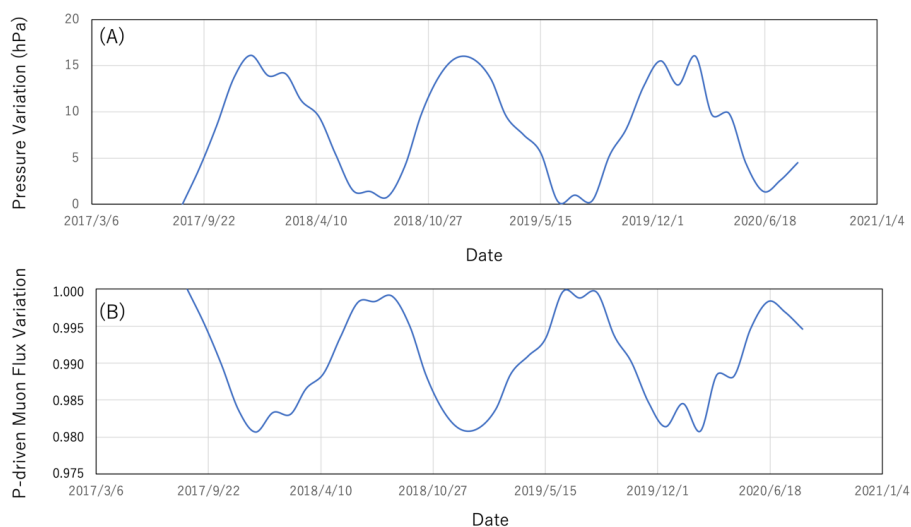
180
181 Figure 2. Variations in the muon flux induced by the ground-level atmospheric pressure
182 variations. The muon flux variations (blue filled circles) are compared with the ground-
183 level atmospheric pressure variations (green solid lines) induced by the 2018 Typhoon
184 No 24 (A). The muon flux variations (blue filled circles) are shown as a function of the
185 ground-level atmospheric pressure. The dotted line indicates the linear function fitted to
186 these data points (B).

187



188

189 With Eq. (1), seasonal variations of the muon flux caused by variations in the ground-
190 level atmospheric pressure (P-driven muon flux variations) were evaluated. Figure 3A
191 shows seasonal variations in the ground-level atmospheric pressure measured at the
192 Kagoshima Meteorological Observatory in the period between August 2017 and August
193 2020. Figure 3B shows the corresponding P-driven muon flux variations based on Eq. (1).
194



195

196 Figure 3. Seasonal variations in the ground-level atmospheric pressure (A) and variations
197 of muon flux due to variations in the ground-level atmospheric pressure (B). The data
198 are shown in the period between August 2017 and August 2020. The ground-level
199 atmospheric pressure data were taken from Reference (Japan Metrological Agency, 2023).

200

201

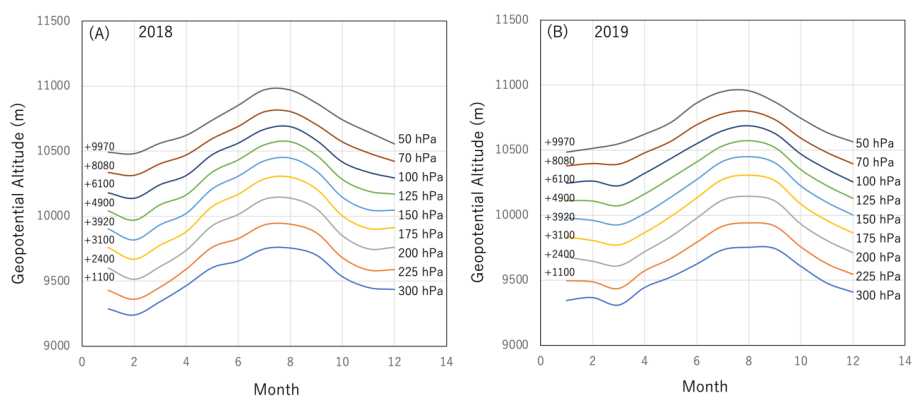
202 3.2 Balloon-based studies near the muopause

203 Japan Meteorological Agency launches a balloon from Kagoshima city twice a day (09:00
204 and 21:00 JST) to monitor the upper atmosphere. The monthly measurement results
205 acquired in 2018 and 2019 are shown in Figure 4. As shown in this figure, the altitude of
206 the muopause varies $\Delta H \sim 500$ m, reflecting seasonal variations (i.e., altitude that
207 increases in the summer time) of the muopause. While the muon generation depth has a
208 certain span (50-300 hPa), as can also be seen in this figure, the isobaric surface height
209 corresponds closely with the variations in this span. Therefore, we can conclude that the
210 isobaric structure of the upper muosphere is simply pushed further from sea level in



211 summer and pushed closer to sea level in winter (dark green ovals in Figure 1B).
212 Consequently, it is expected that variations in the muon survival rate at sea level is a
213 function of the muopause height.

214



215

216 Figure 4. Seasonal changes in the geopotential altitude of the upper troposphere and the
217 lower stratosphere. The data acquired in 2018 (A) and the data acquired in 2019 (B) are
218 shown. The data were taken from the Japan Metrological Agency survey (Japan
219 Metrological Agency, 2023). The numbers on the left side of each panel indicate the offset
220 of the altitude in units of meters.

221

222

223 3.3 Modeling of the seasonal isobaric surface height effect on the muon flux

224 As was described in the previous subsection, the isobaric surface height variations ΔH
225 (H) are independent from H in this span. The modeling procedure is summarized as
226 follows.

227

228 (A) The zenith-angular dependent open-sky muon spectrum data points are taken from
229 various prior experimental works (Allkofer *et al.*, 1985; Haino *et al.*, 2004; L3
230 Collaboration., 2004).

231

232 (B) These muon spectrum data points are interpolated to derive $I_0(E, \theta)$ by using the
233 Thompson and Whalley analytical formula (Thompson and Whalley, 1977).

234

235 (C) Calculations of the angular-dependent muon flux are done, based on the following
236 formula:



237

$$n(\theta, \phi) = \int I(E, \theta) dE, \quad (2 - 1)$$

239

$$I(E, \theta) = I_0(E, \theta) \exp(-\Delta H(\sin \theta)^{-1}/660\gamma(E)[m])(1-\Delta N), \quad (2 - 2)$$

241

242 where E and θ are respectively the muon's energy and the arrival angle from zenith at sea
 243 level, $I_0(E, \theta)$ is the reference muon flux, and γ is the Lorentz factor. Figure 5 plots Eq. (2-
 244 1) for $\Delta H = 0$ m (Figure 5A) and $\Delta H = +500$ m (Figure 5B). The positive and negative
 245 signs attributed to ΔH respectively indicate respectively upward variations and downward
 246 variations. If θ approaches the value of zero, $(\sin \theta)^{-1}$ will be diverged, so in this case, the
 247 spherical curvature of the Earth has to be considered (for $\theta=90^\circ$).

248

249 (D) Calculate the number of muons recorded by the detector with:

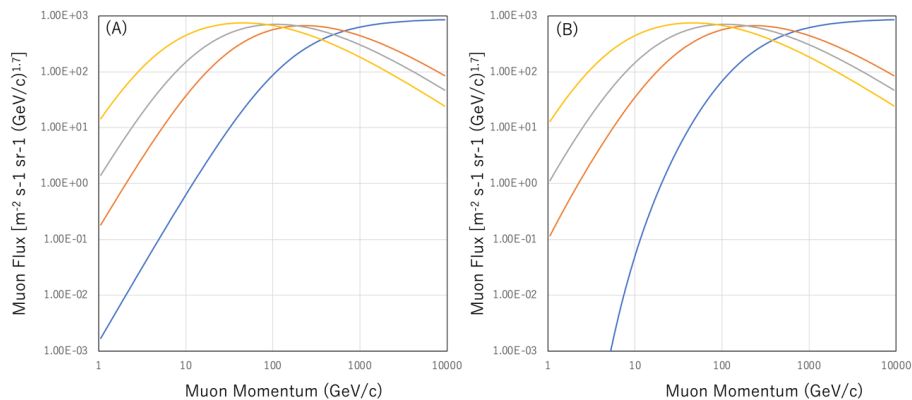
250

$$N = \int_{\phi_0}^{\phi_1} \int_{\theta_0}^{\theta_1} n(\theta, \phi) d\theta d\phi, \quad (3)$$

252

253 where θ_0 , θ_1 , ϕ_0 , and ϕ_1 are respectively the detector's zenith ($\theta_0-\theta_1$) and azimuth ($\phi_0-\phi_1$)
 254 angular acceptance. Eq. (3) was used for the isobaric correction to the muon flux in the
 255 current work.

256



257

258 Figure 5. Differential muon flux for different isobaric surface altitudes. The spectra
 259 calculated for the reference isobaric surface altitude ($\Delta H = 0$ m) are shown in (A) and for
 260 the case when the isobaric surface is uplifted by 500 m in (B) for various muon's arriving



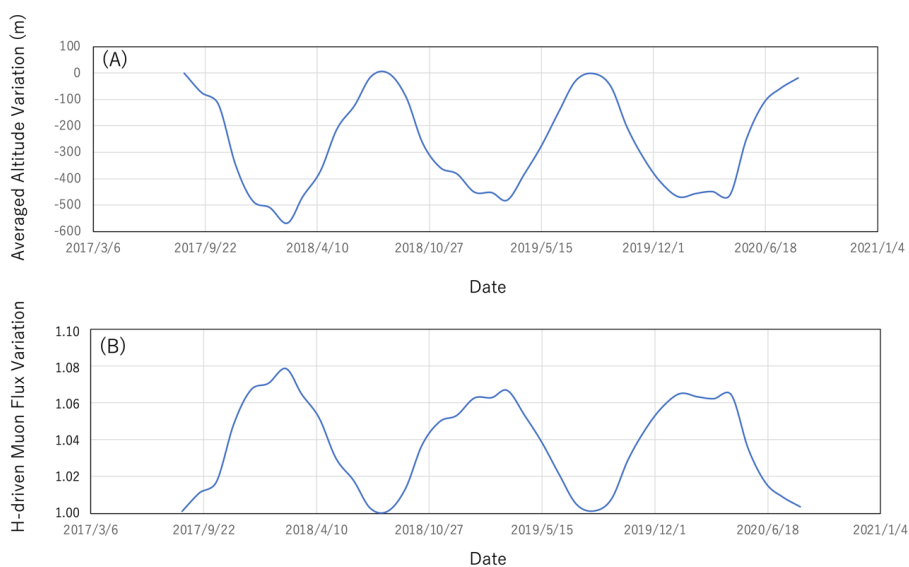
261 angles: 90° (blue), 80° (orange), 70° (gray), and 50° (yellow). Only slanted muons are
262 shown due to the geometrical configuration of the current detector setup (see below).

263

264

265 With Eq. (2-1), seasonal variations of the muon flux due to the isobaric surface height
266 effect (H-driven muon flux variations) were calculated. Figure 6A shows the balloon-
267 based ΔH value averaged over the altitudes which ranged between 50 hPa and 300 hPa.
268 Figure 6B shows the corresponding H-driven muon flux variations based on Eq. (2-1). In
269 order to match the angular acceptance of the racker (described in the next section), the
270 zenith-angular integration range of Eq. (2-1) was set to be 50°-80°. It was assumed that
271 the muon's arriving angles are azimuthally isotropic. These results are subsequently used
272 for the muon flux modeling process which will be described in the following subsection.
273 As can be compared between Figure 4 and Figure 6, the seasonal isobaric surface height
274 effect (up to 8%) is much larger (by a factor of 4) than the seasonal barometric effect (up
275 to 2%).

276



277

278 Figure 6. Balloon-based isobaric height variations averaged over the altitudes between 50
279 hPa and 300 hPa (A) and H-driven variations of the muon flux without the barometric
280 correction (B). The data are shown for the period between August 2017 and August 2020.
281 The balloon-based isobaric height data were taken from Reference (Japan Metrological
282 Agency, 2023).



283

284

285 **4. Apparatus**

286 The muon tracker used in this study consisted of 90 scintillator strip detectors. Each
287 scintillator strip detector consisted of a plastic scintillator (Bicron BC-408) strip
288 connected to a photomultiplier tube (PMT; Hamamatsu R7724) via an acrylic light guide.
289 The typical pulse height outputted from the PMTs were 3-5 V while the threshold level
290 of the discriminator was set to be 50 mV, so that the counting rate would not be easily
291 influenced by the drift of the PMT gain and the discriminator's threshold level caused by
292 variations in ambient temperature. The width and the length of the plastic scintillator strip
293 were respectively 100 mm and 1500 mm. These strips were arranged vertically and
294 horizontally to form three position sensitive detectors (PSDs) Three PSDs were vertically
295 arranged with a spacing of 60 cm. In order to reject electromagnetic components, (such
296 as positrons/electrons) a 10-cm thick lead block and a 3-cm thick stainless-steel with a
297 thickness of 3 cm were inserted into each interval between the PSDs.
298

299 Each of the resultant PSDs consists of a segmented plane with 15×15 segments having
300 a 1.5×1.5 m² active area with a spatial resolution of 10 cm. Since the distance between
301 the uppermost stream detector and the lowermost stream detector is 120 cm, the angular
302 resolution of this detector is 83 mrad. This angular resolution is equivalent to the spatial
303 resolution of 830 m at a location 10 km from the tracker, but it is reduced to 8.3 km at a
304 location 100 km from the tracker. The elevation and azimuth angular acceptance are
305 respectively $0^\circ - 51^\circ$ and $\pm 51^\circ$. However, since the active area is drastically reduced for
306 muons injecting at higher angles with respect to PSD planes (e.g., for muons arriving at
307 an elevation angle of 51° and an azimuth angle of 51° , the tracker's active area is reduced
308 to $1/225$), for practicality, a much smaller angular region ($14^\circ - 32^\circ$ for elevation angular
309 region and $\pm 28^\circ$ for azimuthal angular region) was employed. For tracking, all vertices
310 are examined but only the vertices that are aligned (along a straight line) are counted as
311 an event to ensure that only muons were selected. Lead and stainless-steel shields within
312 the detector decrease the background noise, however they also increase the possibility of
313 muon scattering events. However, these scattering angles (10-20 mrad) are considered to
314 be negligible in comparison to the current tracker's angular resolution (>80 mrad). The
315 muon tracker used in the current experiment was located in Kagoshima city, Japan and it
316 was pointed towards the southern direction. The measurement period was between
317 August 20, 2017- June 30, 2020 (1,044 days).

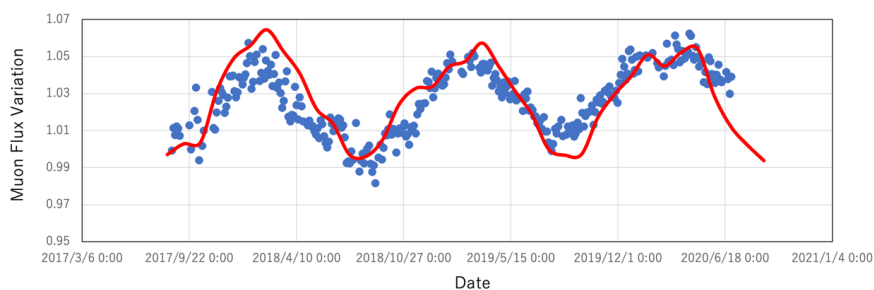


318

319 **5. Comparison between the model and the experimental data**

320 Figure 7 shows the seasonal variation in the muon flux data acquired in the period
321 between August 20, 2017- June 30, 2020. As was expected, the muon flux showed a
322 negative correlation between the ambient temperature and the muon flux, indicating that
323 the isobaric surface height effect is predominant in seasonal variations in the muon flux.
324 In this period there were not any specific extraterrestrial events (such as a Forbush
325 decrease) that could have affected the primary flux. The muon counts in each bin (bin
326 width = 3 days) ranged between 7×10^5 - 7.4×10^5 . The muon flux variations were
327 normalized to the value observed on August 20, 2017. The muon flux modeling results
328 with barometric and isobaric corrections are overlaid on this plot (red solid lines in Figure
329 7). The root mean square (RMS) of the deviations between the theoretical values and the
330 observational values is 0.00987. The measured seasonal variation in the muon flux is well
331 explained by combining the current barometric and isobaric correction models.

332



333

334 Figure 7. Seasonal variation in the muon flux data acquired in the period between August
335 20, 2017- June 30, 2020. The observation values (blue filled circles) and theoretical
336 values (red solid lines) are shown. The statistical errors associated with each data point
337 fit within the size of the circles.

338

339

340 **6. Limitations and potential improvements**

341 The RMS deviation of the observed muon flux variations from the DoF modeling results
342 ($\sim 1\%$) induces an error of ~ 60 m in the estimation of the muopause height with the DoF
343 technique. The DoF time resolution is 3 days. These characteristics, the accuracy and time
344 resolution, are both significantly lower than the accuracy and the time resolution that can



345 be attained with the GPS-loaded balloons (~5 m and 1 second). This is the main
346 limitations of the DoF approach in its current stage of development. These limitations
347 mainly come from (A) the statistics and (B) the modeling accuracy. Regarding factor (A),
348 the detector size needs to be enlarged to record more muon events. In order to confirm
349 this detector size effect, further DoF measurements with larger sized detector (4.5 m²) are
350 currently ongoing. Regarding factor (B), more precise modeling developments are
351 ongoing with the extended air shower (EAS) Monte Carlo (MC) simulation. The current
352 work is based on the assumption is that the muons travel straight forwardly without
353 experiencing scatterings; however, it must be noted that after the muons are generated
354 near the tropopause, they travel through a material with a thickness equivalent to 20-meter
355 water equivalent (m.w.e.) - 40 m.w.e. for the muons arriving from an elevation angular
356 region between 14 °- 32 °, having a tendency to scatter to cause longer track lengths in the
357 troposphere. This effect must be taken into account in our future work to make
358 improvements to factor (B). The discrepancy between the balloon position and the muon
359 generation region may also influence how closely the compared data sets match. The
360 muospheric layer thickness seasonally oscillates, but its amplitude is likely to depend on
361 location of the measurement on the Earth since the near surface temperature is regionally
362 varied. If the surface temperature is different between the location underneath the ballon
363 and the location underneath the region of interest of the muopause, the muopause height
364 in this region and the balloon-based isobaric surface altitude will not coincide. Since the
365 balloon's trajectory is random, and it is difficult to control it, the next step in development
366 is to compare the DoF data with the satellite-based stratospheric sensing data.

367

368 **7. Conclusion**

369 In conclusion, a new muographic technique called DoF was proposed, and with this
370 technique, it was found that the muopause height interlocks with the isobaric surface
371 height in the upper troposphere and lower stratosphere. This work defined (A) the position
372 of the muopause and the layer span of the muosphere on the Earth; additionally, it was
373 shown that (B) the muopause is located in the lower stratosphere, (C) seasonal variations
374 in the muon flux are predominantly ruled by muopause dynamics, (D) muopause
375 dynamics can be visualized with LOF muography by taking advantage of directional
376 patterns of cosmic-ray muon's survival probabilities, and (E) muopause dynamics is
377 closely related with isobaric surface height variations in the lower stratosphere.

378

379 Muopause dynamics has the potential to contribute to research focused on the upper
380 tropospheric and lower stratospheric dynamics. In future studies, the potential of LOF



381 muography for application to studying the dynamical processes occurring in the upper
382 troposphere and lower stratosphere will be further investigated by performing related case
383 studies and making specific comparisons with other atmospheric climate datasets.

384

385

386 REFERENCES

387 Adamson, P. et al. (MINOS Coll.: Observation of muon intensity variations by season
388 with the MINOS far detector, *Phys. Rev.*, D81, 012001,
389 doi:10.1103/PhysRevD.81.012001, 2010

390

391 Allkofer, O.C. *et al.* Cosmic ray muon spectra at sea-level up to 10 TeV. *Nucl. Phys. B*
392 **259**, 1-18 (1985).

393

394 Blackett, P. M. S. On the instability of the Barytron and the temperature effect of cosmic
395 rays. *Phys. Rev.* **54**, 973–974 (1938). <https://doi.org/10.1103/PhysRev.54.973>

396

397 Boezio M. *et al.* New Measurement of the Flux of Atmospheric Muons. *Phys. Rev. Lett.*
398 **82**, 4757 (1999).

399

400 Boezio M. *et al.* Measurement of the flux of atmospheric muons with the CAPRICE94
401 apparatus. *Phys. Rev. D* **62**, 032007 (2000).

402

403 COSINE-100 Collaboration. Measurement of the cosmic muon annual and diurnal flux
404 variation with the COSINE-100 detector (2020). Retrieved from
405 <https://arxiv.org/abs/2005.13672>

406

407 Dmitrieva, A.N. *et al.* Corrections for temperature effect for ground-based muon
408 hodoscopes. *Astropart. Phys.* **34**, 401-411 (2011).

409

410 Gnanvo, K. *et al.* Imaging of high-Z material for nuclear contraband detection with a
411 minimal prototype of a muon tomography station based on GEM detectors. *Nucl. Instr.*
412 *Meth. A* **652**, 16-20 (2011).

413

414 Haino, S. *et al.* Measurements of primary and atmospheric cosmic-ray spectra with the
415 BESS-TeV spectrometer. *Phys. Lett. B* **594**, 35-46 (2004).

416



- 417 Japan Meteorological Agency. Past Meteorological Data (2023). Retrieved from
418 <https://www.jma.go.jp/jma/indexe.html>.
419
- 420 Kretschmer, M. *et al.* The different stratospheric influences on cold extremes in Eurasia
421 and North America. *npj Clim. Atmos.* **1**, 44 (2018).
422
- 423 L3 Collaboration. Measurement of the atmospheric muon spectrum from 20 to 3000 GeV.
424 *Phys. Lett. B* **598**, 15-32 (2004)
425
- 426 Millán, L. *et al.* The Hunga Tonga - Hunga Ha'apai Hydration of the Stratosphere,
427 *Geophys. Res. Lett.* **49**, e2022GL099381 (2022).
428
- 429 Morishima, K., Kuno, M., Nishio, A. *et al.* Discovery of a big void in Khufu's Pyramid
430 by observation of cosmic-ray muons. *Nature* **552**, 386–390 (2017).
431 <https://doi.org/10.1038/nature24647>
432
- 433 Myssowsky, L., & Tuwim, L. Unregelmäßige intensitätsschwankungen der
434 höhenstrahlung in geringer seehöhe. *Z. Phys.* **39**, 146–150 (1926).
435 <https://doi.org/10.1007/BF01321981>
436
- 437 Particle Data Group, The Review of Particle Physics. *Prog. Theor. Exp. Phys.* **2022**,
438 083C01 (2022).
439
- 440 Tanaka, H. K. M., Kusagaya, T. & Shinohara, H. Radiographic visualization of magma
441 dynamics in an erupting volcano. *Nat. Commun.* **5**, 3381 (2014).
442 <https://doi.org/10.1038/ncomms4381>
443
- 444 Tanaka, H. K. M., Gluyas, J., Holma, M. *et al.* Atmospheric muography for imaging and
445 monitoring tropic cyclones. *Sci. Rep.* **12**, 16710 (2022a). <https://doi.org/10.1038/s41598-022-20039-4>
446
- 447
- 448 Tanaka, H. K. M., Aichi, M., Balogh, S.J. *et al.* Periodic sea-level oscillation in Tokyo
449 Bay detected with the Tokyo-Bay seafloor hyper-kilometric submarine deep detector (TS-
450 HKMSDD). *Sci. Rep.* **12**, 6097 (2022b). <https://doi.org/10.1038/s41598-022-10078-2>
451
- 452 The IceCube Collaboration. Seasonal variation of atmospheric muons in IceCube (2019).



453 Retrieved from <https://par.nsf.gov/servlets/purl/10171530>
454
455 Thompson, M. G. & Whalley, M. R. The sea-level muon spectrum and charge ratio and
456 their relationship with high-energy accelerator data. *J. Phys. G* **3**, 97 (1977).
457
458 Tilav, S. et al. Atmospheric variation as observed by IceCube (2010). Retrieved from
459 arXiv:1001.0776.
460
461 Vömel, H. *et al.* Water vapor injection into the stratosphere by Hunga Tonga-Hunga
462 Ha'apai, *Science* **377**, 1444–1447 (2022).
463
464 Yook, S. *et al.* Climate Impacts and Potential Drivers of the Unprecedented Antarctic
465 Ozone Holes of 2020 and 2021. *Geophys. Res. Lett.* **49**, e2022GL098064 (2022).
466 <https://doi.org/10.1029/2022GL098064>
467
468
469

470 **Data Availability**

471 The datasets used and/or analyzed during the current study are available from the
472 corresponding author on reasonable request.

473

474 **Author Contribution**

475 H.K.M.T. wrote the text. H.K.M.T. prepared the figures. H.K.M.T. reviewed the
476 manuscript.

477

478 **Competing interests**

479 The author is a member of the editorial board of Geoscientific Instrumentation, Methods
480 and Data Systems.

481

482

483

484

485